



# Global Analysis of Transitional Flow Over a Cone-Flare at High Mach Numbers

Cole Sousa,\*Guillaume Grossir,\*Olivier Chazot,\*Stuart Laurence§

#### Abstract

Experiments are conducted in the VKI Longshot facility to investigate the development of boundary-layer and shear-layer disturbances over a slender cone/flare geometry at high hypersonic Mach numbers ( $M \gtrsim 12$ ). Both attached ( $+5^{\circ}$  flare) and separated ( $+15^{\circ}$  flare) cases are examined using a high-speed calibrated schlieren diagnostic; a super-temporal reconstruction technique enables global measurements over all relevant frequencies. Second-mode waves play an important role in both configurations. For the attached case, these waves undergo significant amplification at the corner and experience further growth at higher frequencies downstream. The corner also leads to the rapid onset of flow features at second-mode super-harmonic frequencies. For the separated case, the second mode waves propagate along the shear layer and are then highly distorted by passage through the reattachment location, where substantial excitation over all frequencies is observed. Lower-frequency shear-layer disturbances also exhibit rapid growth above the separation bubble in this configuration. These disturbances radiate strongly to the outer flow, leading to growing, large-scale perturbations of the separation shock. Significant propagation of second-mode energy along the various shocks in both configurations is also noted, and appears to be somewhat more prominent than in earlier experiments at lower hypersonic Mach numbers.

Keywords: Boundary-layer transition, shock-wave/boundary-layer interaction, flow visualization

### Nomenclature

Latin u – Flow velocity

f - Frequency y - Approximate distance above cone surface

 $\begin{array}{lll} {\rm h\,-\,Enthalpy} & {\rm Greek} \\ {\rm N\,-\,N\text{-}factor} & \rho - {\rm\,Density} \end{array}$ 

p – Pressure Subscripts

 $Re_m$  – Unit Reynolds number 0 – Stagnation conditions s – Approximate distance along cone surface  $\infty$  – Freestream conditions

 $\mathsf{T}-\mathsf{Temperature}$   $i-\mathsf{Most}$  upstream location

### 1. Introduction

The design of practical hypersonic vehicles is constrained by the extreme thermal and mechanical surface loads which occur when travelling within the stratosphere at high Mach numbers. These concerns are further aggravated by the dramatic increase in surface heat flux and skin friction which accompanies the laminar-turbulent transition of the vehicle boundary layer. Due to incomplete understanding of the hypersonic transition process and inadequate modeling capabilities, these issues are presently avoided by over-designed thermal protection systems; however, such overdesigned systems come with

<sup>\*</sup>University of Maryland, College Park, Department of Aerospace Engineering, College Park, MD 20742, colesousa33@qmail.com

<sup>†</sup>von Karman Institute for Fluid Dynamics, Chaussée de Waterloo 72, 1640 Rhode-St-Genèse, Belgium, guillaume.grossir@vki.ac.be

<sup>&</sup>lt;sup>‡</sup>von Karman Institute for Fluid Dynamics, Chaussée de Waterloo 72, 1640 Rhode-St-Genèse, Belgium, olivier.chazot@vki.ac.be

<sup>§</sup>University of Maryland, College Park, Department of Aerospace Engineering, College Park, MD 20742, stuartl@umd.edu

significant weight penalties, placing undesirable restrictions on the vehicle and mission. Safe and efficient vehicle design thus requires significant advances in our understanding of the underlying physics of hypersonic boundary-layer transition.

In the low-disturbance environments typical of hypersonic flight and most ground-test facilities, boundary-layer transition on slender, smoothly varying bodies is characterized by the linear growth of instabilities within the boundary-layer, followed by nonlinear modal interactions and breakdown (Fedorov, 2011). The outer mold line of true flight vehicles does not always vary smoothly in the streamwise direction, however, and may exhibit sudden changes in angle, e.g., at control surfaces or the intake. An increase in angle will introduce a shock wave and accompanying shock-wave/boundary-layer interaction (SWBLI). These SWBLIs not only affect disturbances propagating from the upstream boundary layer (Balakumar et al., 2002; Novikov et al., 2016; Lugrin et al., 2020) but can also give rise to new instability mechanisms, particularly associated with the emergence of the shear layer in the separated case (Roghelia et al., 2017; Guiho et al., 2016; Sidharth et al., 2018) and Görtler vortices associated with streamline curvature in the SWBLI region (Saric, 1994).

Regarding the incoming disturbances, on a slender, sharp geometry at small angles of incidence, the dominant boundary-layer instability mechanism will change from oblique, first-mode waves (the compressible analog of Tollmien-Schlichting waves) to two-dimensional second-mode waves as the Mach number is increased above values of approximately 4 (Mack, 1975). These two instability types have distinct physical natures: first-mode waves are vortical disturbances, while second-mode waves are primarily acoustic in nature (Fedorov and Tumin, 2011) (though it has recently been shown that they also produce non-zero vortical fluctuations (Unnikrishnan and Gaitonde, 2020)). Second-mode waves exhibit extremely high frequencies (hundreds of kHz to MHz (Parziale et al., 2014; Laurence et al., 2016; Casper et al., 2016; Kennedy et al., 2018; Craig et al., 2019), compared to tens of kHz for first-mode waves); their amplification rates peak near Mach 6 and thereafter decrease with further increases in Mach number (Mack, 1975).

Regarding the separated shear layer, the stability of a compressible free shear layer was first investigated by Lees and Lin (1946) and later received much attention in the context of fuel-air mixing inside scramjet engines, e.g., Zhuang et al. (1988); Jackson and Grosch (1989b); Balsa and Goldstein (1990); Jackson and Grosch (1990). Among the salient conclusions from these earlier studies for the present investigation are that, above a certain relative Mach number of the two streams, there are two groups of unstable modes (referred to as fast and slow), both of which are vortical in nature. Maximum amplification rates tend to decrease with Mach number to a certain point, and then increase thereafter. Increasing the relative temperature of the slower stream significantly decreases amplification rates, and also shifts this reversal Mach number to higher values.

Although the nature of the incoming disturbances and the shear-layer instabilities are reasonably well understood in isolation, only recently have researchers begun to probe how they might interact and compete in leading to transition in the practical context of a high-speed compression-corner flows. In computations of a 5.5° compression at Mach 5.4, Balakumar et al. (2002) found second-mode waves to be neutrally stable while traversing the separation region, while a lower-frequency unstable mode was associated with the shear layer itself. Direct numerical simulations of the same configuration by Novikov et al. (2016), however, found significant forcing of second-mode wavepackets downstream of reattachment, leading to transition. Lugrin et al. (2020) performed a "quasi-direct numerical simulation" of a laminar boundary layer encountering an axisymmetric 15° compression ramp at Mach 5, observing a transition process dominated by streamwise streaks resulting from the nonlinear interaction of oblique first-mode waves. A related configuration, that of a cone-cylinder-flare, has recently received attention both in wind-tunnel experiments and computations (Benitez et al., 2020, 2021; Paredes et al., 2022). Interpretation of the incoming disturbance behavior is somewhat complicated in this configuration, however, by their passage through the expansion at the cone-cylinder junction before reaching the compression corner. Recent experiments have also been performed at Mach 6 in the UMD Hyper-TERP shock tunnel (Butler and Laurence, 2021b,a) to examine the transition process over a sharp, 5° cone/flare with varying compression angles, intended to induce flows ranging from fully attached to sub-

Run Number	Flare angle	$M_\infty$	$Re_m$	$h_0$	$p_0$	$ ho_{\infty}$	T <sub>∞</sub>	U∞
	[°]		$[10^6/m]$	[MJ/kg]	[MPa]	$[kg/m^3]$	[K]	[m/s]
1878	5	12.0	1.95	3.11	37.2	0.0056	102	2450
1877	15	13.1	2.93	2.79	58.3	0.0072	76	2326

Table 1. Average freestream conditions during the test window used for the schlieren analysis

stantially separated. An ultra-high-speed schlieren diagnostic, combined with global analysis techniques - spectral proper orthogonal decomposition (SPOD) and bispectral analysis - allowed the increased dominance of shear-layer disturbances over second-mode disturbances as the flare angle was increased to be observed and the investigation of nonlinear interactions involving the various disturbances.

The various studies just described have primarily been performed in the low hypersonic regime, meaning that the influence of Mach number on the development and interplay of the various disturbance types present, and ultimately the transition process, remains unexplored. In this work, we therefore conduct an experimental study of the flow over a cone/flare geometry at much increased ( $\gtrsim$ 12) Mach numbers. High-speed calibrated schlieren enables a global picture of the development of the instabilities present for both attached and fully separated flows.

### 2. Experimental Methodology

### 2.1. Facility

All experiments were performed in the Longshot gun tunnel at the von Karman Institute for Fluid Dynamics (VKI). The Longshot operates via adiabatic compression of the driven gas (here pure nitrogen) by an inertial piston. A set of 48 check valves located at the end of the driven tube are used to trap the gas in the reservoir at peak stagnation conditions. This mechanism extends the useful test time by an order of magnitude but results in a finite amount of compressed gas in a constant volume reservoir, leading to a temporal decay of stagnation conditions during the run. For the set of experiments reported herein, a contoured nominally Mach-14 nozzle with a 541 mm exit diameter expands the test gas to the desired conditions. Detailed characteristics of the Longshot tunnel compression process have been reported in detail by Grossir and Ilich (2018).

Two shots performed in the current campaign are reported here. Although all experiments were at the same nominal test condition, the operating principle of Longshot introduces significant run-to-run variation. The freestream Mach number and unit Reynolds number [1/m], along with other relevant flow quantities, are shown in table 1 for each shot during the utilized test time of approximately 4.5 ms. The determination of freestream flow properties relies on measurements taken with three intrusive probes placed beside the main test article during each shot: a freestream static pressure probe, a Pitot pressure probe, and a stagnation point heat-flux probe. A full description of the modelling and numerical methods used to estimate the freestream properties from these measurements has been described by Grossir et al. (2018).

#### 2.2. Test Article

A cone-flare geometry of overall length 486.2 mm, identical to that used in Butler and Laurence (2021a) was employed as the test article for this campaign. The model is composed of a sharp stainless steel conical nose tip followed by a primary  $5^{\circ}$  half-angle stainless steel conical frustum and an interchangeable secondary polyetheretherketone (PEEK) conical frustum of increased half-angle. The nose-tip radius was previously measured as 0.10 mm. Flare half-angles of  $10^{\circ}$  and  $20^{\circ}$  were used in shots 1878 and 1877, respectively, corresponding to axisymmetric compression angles of  $+5^{\circ}$  and  $+15^{\circ}$  (hereinafter, we refer to individual shots by the relevant compression angles), starting 410 mm downstream of the nosetip. A diagram of the model with the  $+15^{\circ}$  compression is shown in figure 1. Additional experiments were performed with a  $+10^{\circ}$  compression, but these will not be described here.

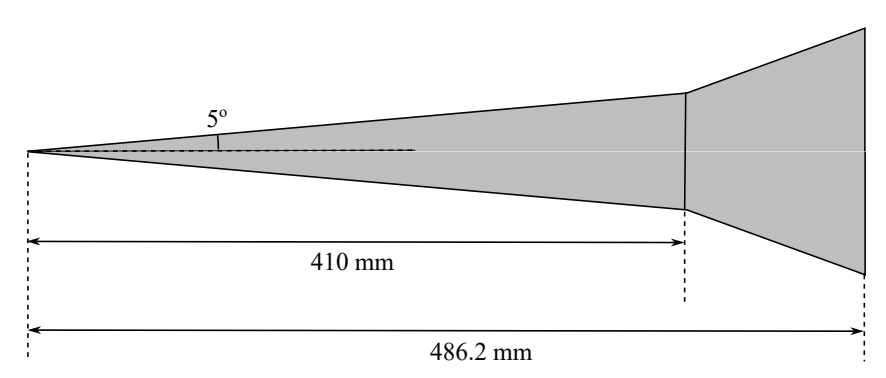


Fig 1. Sketch of the cone/flare test article with the  $+15^{\circ}$  flare installed.

#### 2.3. Schlieren Measurements

## 2.3.1. Apparatus

The primary diagnostic for these experiments was high-speed calibrated schlieren, performed using a folded three-mirror Z-type setup. Light emitted from a Cavilux HF laser operating at 640 nm with a 30 ns pulse width was first collimated to run parallel to the tunnel by a 450 mm diameter parabolic mirror with a focal length of 3000 mm. The light path following this first mirror is parallel to the tunnel flow direction. The light was then deflected by  $45^{\circ}$  into the test section by a large planar mirror (610 mm diameter). Light leaving the test section was focused using a 420 mm diameter parabolic mirror, also with a focal length of 3000 mm, and captured with a Phantom v2012 high-speed camera. The camera alignment was modified for each run such that the compression corner was located approximately in the bottom centre of the camera field of view and the camera roll angle was set at an intermediate value between the frustum and flare half-angles to maximize the streamwise view of the model boundary layer. A horizontal knife-edge cutoff was used to visualize the density gradients approximately normal to the model surface. A frame rate of 500 kHz with an image resolution of  $640 \times 48$  pixels and an image scale of 0.200 mm/pixel was used for both experiments described herein. A calibration procedure employing a long-focal-length lens was employed to convert the image intensities into integrated density gradients (Kennedy et al., 2018).

#### 2.3.2. Super-Temporal Reconstruction

In order to facilitate analysis of high-frequency content present in the pixelwise temporal signals, the reconstruction procedure described in Sousa and Laurence (2025) was performed on the schlieren video data. This technique utilizes the measured disturbance velocities (speeds and directions) together with information from neighbouring pixels to "fill in" the temporal signal between time steps for a given pixel. The Nyquist limit of the camera frame rate is thus bypassed and replaced with the spatial Nyquist limit of the image resolution. When applied to the current experiments, the resulting sampling rates are over 6 MHz in each case, enabling the analysis of high-frequency second-mode content, including harmonics, that would otherwise be precluded. In Sousa and Laurence (2025), it was also shown that the de-aliasing of the signals by the reconstruction technique improves the measurement accuracy at frequencies below the temporal Nyquist limit.

The relevant disturbances employed for the reconstruction technique were second-mode waves, as these were typically found to dominate the flowfield. For the  $+15^{\circ}$  compression, low-frequency shear-layer disturbances were also present, but these were at sufficiently low frequencies that the original pixel signals could also be used. Propagation velocities were determined using the correlation procedure outlined in Sousa and Laurence (2025). For each experiment, velocities across the entire field were computed by cross-correlating a large number of image pairs taken from the nominal test time. These were biased towards second-mode velocities by first filtering images around the approximate second-mode frequency band.

#### 3. Results

# 3.1. Schlieren Sequences

To begin, we present image sequences from each experiment to give the reader a visual representation of the general time-resolved flow behaviour. These are displayed in figures 2 and 3, which depict reference-subtracted images taken within the useful test time. Every fourth image is shown, resulting in a time interval of 8.00  $\mu$ s; the flow is moving left to right and solid black lines indicate the model surface.

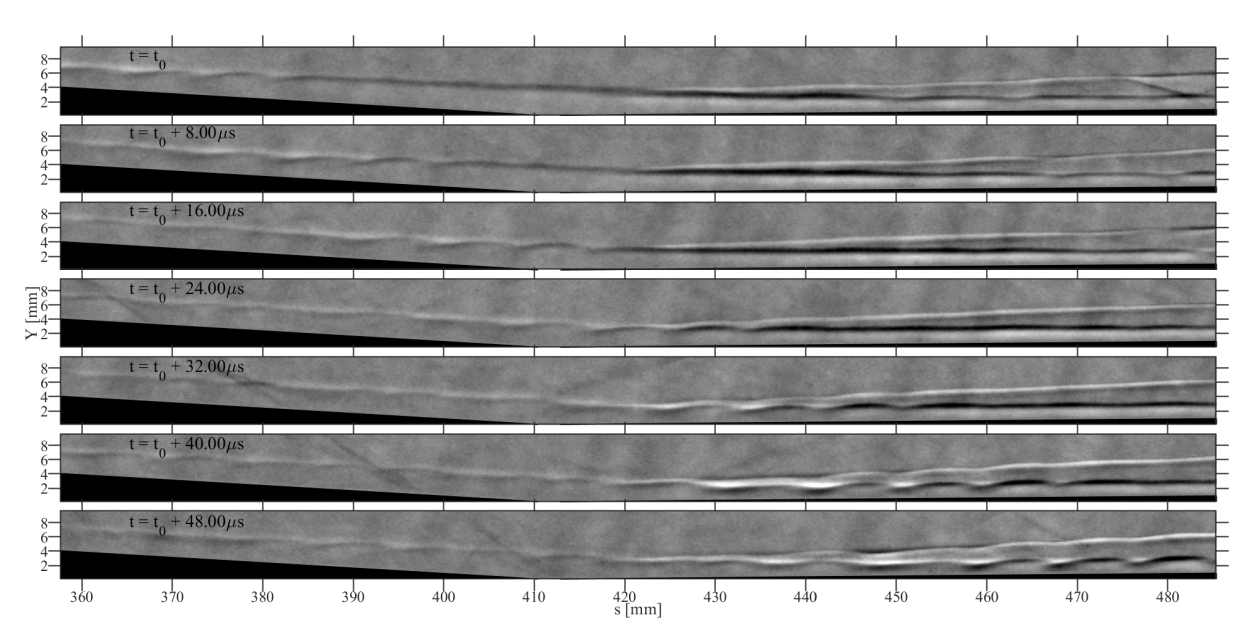


Fig 2. Schlieren image sequence for the  $+5^{\circ}$  compression.

Starting with the  $+5^{\circ}$  compression, a second-mode wave packet can be seen entering the field of view in the first image, with a leading wave located at approximately s=385 mm. This wave packet propagates downstream and reaches the corner at s=410 mm approximately 16  $\mu$ s later. The attached shock wave can be seen to emerge from the incoming boundary-layer edge near s=420 mm. As the second-mode wave packet propagates through this shock, the amplitude of its density fluctuations can be seen to grow substantially. The wave packet continues to propagate within the flare boundary layer and leaves the field of view before experiencing breakdown. Additionally, the interaction of the wave packet with the attached flare shock produces perturbations of approximately the same wavelength that propagate downstream along the shock; similar "radiation" of disturbance energy along shock waves was noted by Butler and Laurence (2021a) at Mach 6.

In the  $+15^{\circ}$  sequence (figure 3), it is clear that this compression angle produces a relatively large separation region, which is bounded by separation and reattachment shocks that leave the relevant boundary layers near s=360 mm and s=440 mm. As the second-mode wave packet passes through the interaction region in this sequence, weak perturbations are produced along the separation shock as the wave packet passes the separation location; the wave packet continues to propagate along the separated shear layer and appears to radiate further energy out to the separation shock, strengthening these perturbations. This radiation may also indicate that the wave packet is travelling supersonically with respect to the mean flow about the shear layer Butler and Laurence (2021a). Upon reaching the reattachment location, the wave packet undergoes significant distortion, with smaller-scale structures developing between the primary periodic features. We also note that the wave packet excites fluctuations along the reattachment shock, which in the last image appear to combine with the existing perturbations on the separation shock. In addition to the second-mode waves, additional, longer-frequency disturbances are visible along the separated shear layer (for example, in the first two images in the sequence); these can

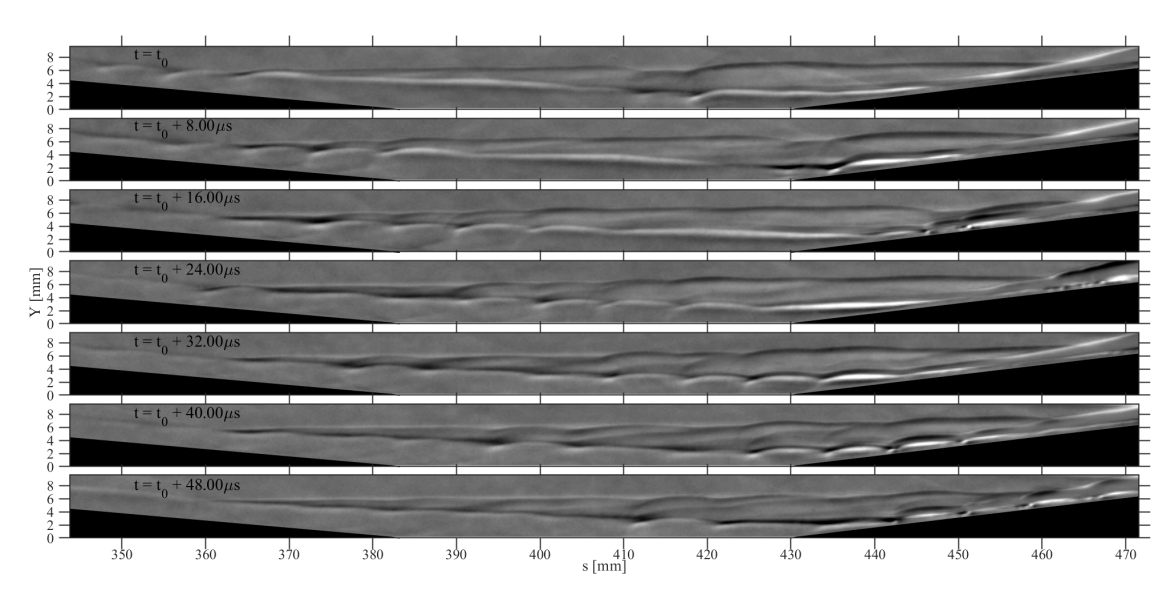


Fig 3. Schlieren image sequence for the  $+15^{\circ}$  compression.

be associated with the shear-layer disturbances noted at Mach 6 by Butler and Laurence (2021a).

## 3.2. Pixel-wise Spectral Analysis

We first examine pixel-wise power spectral densities at select locations within the schlieren field of view to provide the reader with a general idea of the frequency content for the attached and separated flowfields. Three locations are chosen for the smaller flare angle: (1) at the boundary-layer edge of the frustum, upstream of any influence from the compression corner, (2) at the boundary-layer edge of the flare, and (3) along the flare shock. For the larger flare angle, we add two further probe locations: (4) along the separation shock and (5) along the shear layer above the separation bubble. The specific points are indicated by markers in the upper part of figure 4. The boundary-layer edges and shocks were determined here using a Canny edge-detection algorithm. Power spectral densities (PSDs) at these locations for the two compression angles are presented in the lower part of figure 4. In each case, a PSD taken at a pixel in the top-centre portion of the field of view, above any prominent flow features (labelled "freestream" but really in the shock layer behind the attached conical shock) is also included as a baseline. Welch's method is used for the PSD estimate of each signal, using segments of length 1080 with 50% overlap (totaling 49 averaged segments) and a Blackman window function. Data from a total of 2250 raw frames are included, which increases to approximately 27,000 frames using the reconstruction technique. The peaks near 430 kHz are artifacts generated by the reconstruction procedure due to the presence of a moving fringe-like pattern in the raw schlieren videos, likely from the laser light source. A detailed discussion of how such artifacts can be produced by the reconstruction procedure can be found in Sousa and Laurence (2025).

For the  $+5^{\circ}$  flare, a second-mode peak appears near 225 kHz for all non-freestream probe locations. This peak grows significantly between the cone and flare boundary-layer probe locations, remaining well defined, and amplification at higher frequencies is modest. This indicates the flow on the flare remained laminar and second-mode dominated, consistent with schlieren video observations. There is also a clear second-mode peak at the flare-shock probe location with a peak power that is in between those found on the cone and flare boundary layer probe locations. We thus see that the radiation of energy occurs primarily over the same frequency range as the exciting waves. For the  $+15^{\circ}$  flare, second-mode content is again present at all non-freestream probe locations. The spectrum of the additional probe on the separation shock appears to lie very closely to that of the cone boundary layer, though with some additional low-frequency content washing out the second-mode peak slightly. A small additional peak is seen near 70 kHz, whose origin we will return to shortly. The spectra for the shear layer and reattachment shock exhibit elevated broadband content compared to the upstream probe and are

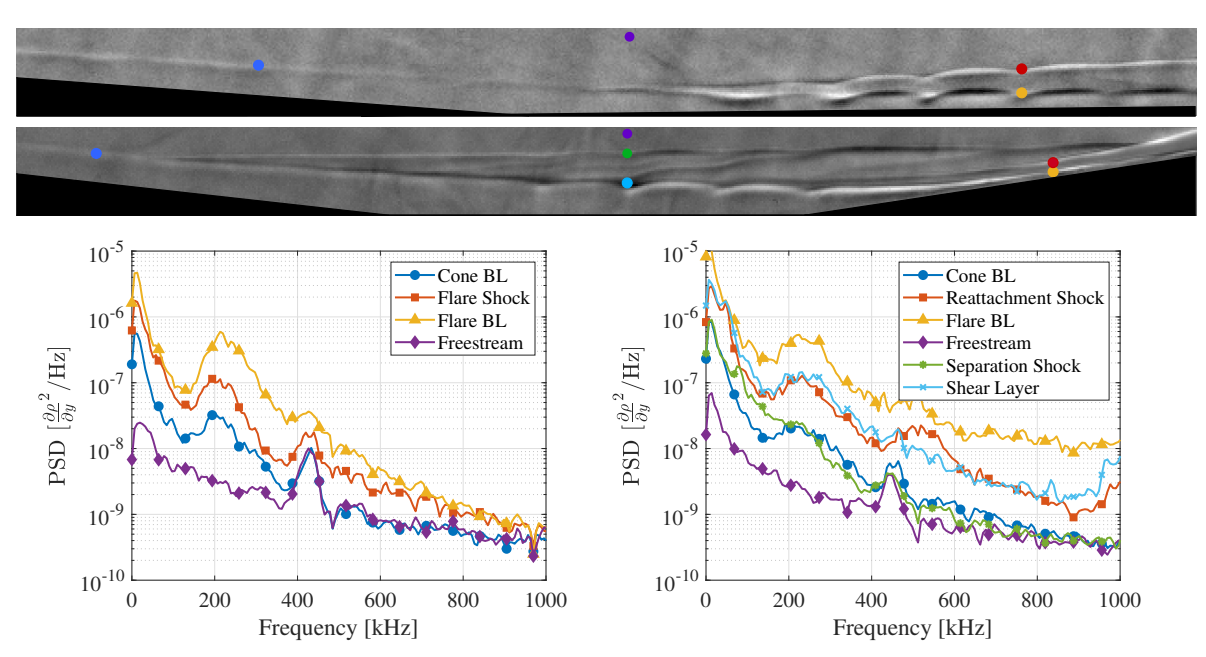


Fig 4. (Top) Locations of selected pixelwise PSDs for the  $+5^{\circ}$  and  $+15^{\circ}$  flares, overlaid on a reference-subtracted image in each case; (bottom) PSDs at the selected pixel locations for compression angles of (left)  $+5^{\circ}$  and (right)  $+15^{\circ}$ .

generally very similar to one another, potentially indicating that incoming disturbances on the shear layer are being directly transmitted along the reattachment shock. Both also show a small peak near 50 kHz, which can be associated with the shear-layer disturbances noted earlier (see also Butler and Laurence 2021a). The flare-probe spectrum shows that reattachment again amplifies a broad range of frequencies and potentially pushes the flow closer to turbulence, though no evidence of the shear-layer disturbance is seen at this location.

To gain a better picture of the spatial distributions of disturbance power over selected frequency bands of interest, in figure 5 we show the integrated PSD in the band 200-250 kHz (to isolate the second-mode fundamental peak) for both compression angles. Dashed lines indicate the wall-normal height within the boundary layer of the most-amplified fundamental content at each streamwise position (i.e., pseudo-streamline of maximum second-mode power). For the smaller flare angle, there is a band of elevated disturbance levels within the boundary layer of the primary cone frustum leading into the compression corner. The disturbance power is then rapidly amplified at the corner and bifurcates into two prominent branches along the flare boundary layer and shock. The strength along the boundary-layer branch remains relatively constant, whereas the shock branch experiences slight decay. For the larger flare angle, the second-mode energy stays largely confined to the shear layer, where it appears to undergo modest amplification before reaching a maximum near reattachment. Some energy is seen emanating along the reattachment shock further downstream. There is a broad region of elevated energy in this frequency range between the shear layer and separation shock, likely produced by the second-mode radiation in this area noted earlier, but there is no appreciable concentration of energy at the separation shock that should result if perturbations of the shock within this frequency band were being generated.

In figure 6, we show similar distributions for the 30 to 80 kHz band, i.e., encompassing the frequency range of the shear-layer disturbances seen for the  $+15^{\circ}$  flare in figure 4. For the  $+5^{\circ}$  flare, we again observe a concentration of energy within the upstream boundary layer, which once more jumps and bifurcates at the corner. There is little evidence of growth in either of these upstream or downstream regions, however. The  $+15^{\circ}$  case is somewhat more interesting. Here, the disturbances experience

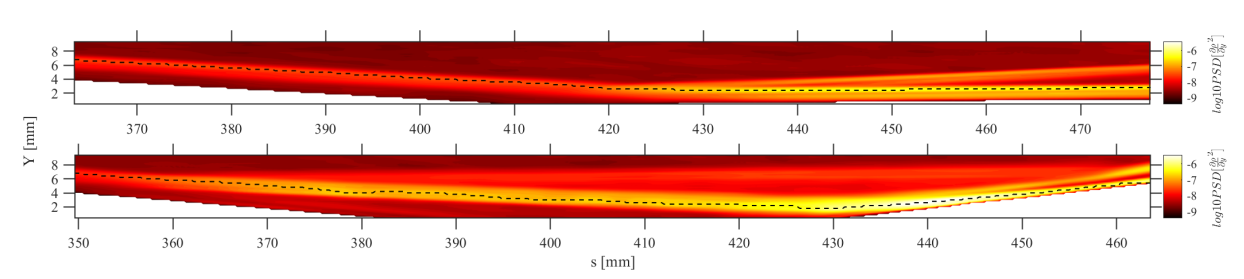


Fig 5. Spatial distribution of the integrated power spectral density over the 200-250 kHz band for compression angles of  $+5^{\circ}$  (top) and  $+15^{\circ}$  (bottom).

strong amplification along the shear layer, reaching a peak just upstream of reattachment. Some energy remains in the flare boundary layer, but at least a comparable fraction appears to emanate along the reattachment shock. Again there is modestly elevated energy between the shear layer and separation shock, but now a clear concentration of integrated power is observed along the shock, essentially creating a second "pseudo-streamline" along which growth is observed. Note that the shear-layer disturbances are likely propagating at a different speed from the second-mode value assumed in the reconstruction Butler and Laurence (2022), meaning there is the potential for erroneous results in the reconstructed signals. To check this, in figure 7 we show the same distribution, but now derived from the raw pixel signals (since 80 kHz lies well below the Nyquist frequency of the camera frame rate). We observe very similar behaviour to the reconstructed map in figure 6: in particular, we again note the second "pseudo-streamline" along the separation shock, which is now explicitly indicated. We thus conclude the the reconstructed signals can be expected to give reliable results, even in this low-frequency range.

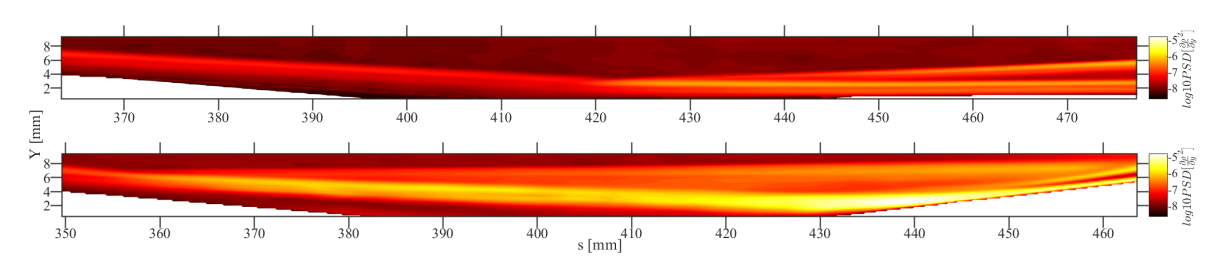


Fig 6. Spatial distribution of the integrated power spectral density over the 30-80 kHz band for compression angles of  $+5^{\circ}$  (top) and  $+15^{\circ}$  (bottom).

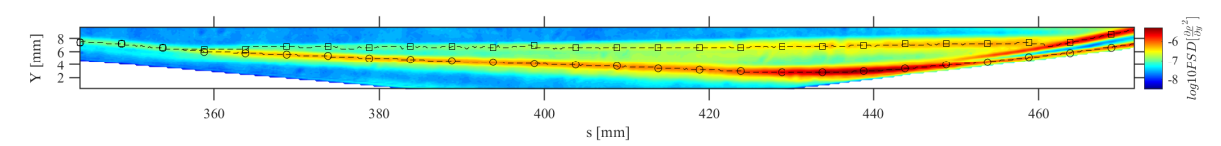


Fig 7. Spatial distribution of the integrated power spectral density over the 30-80 kHz band, computed from the raw video data of the  $+15^{\circ}$  configuration.

Now to depict the spatial development of the disturbances over the entire frequency range, in figure 8 we show the PSD spectra and corresponding frequency-resolved N-factors changes along the second-mode pseudo-streamline for the  $+5^{\circ}$  compression. The N-factor change here is defined as:

$$\Delta N(f,s) = \frac{1}{2} \ln \frac{PSD(f,s)}{PSD(f,s_i)},\tag{1}$$

where  $s_i$  is the most-upstream position visible in the field of view. The dominant content in the frustum boundary layer is in the second-mode range (gradually decaying in frequency moving downstream

as the boundary layer grows) and at lower frequencies ( $\lesssim$ 50 kHz). All frequencies are then amplified upon encountering the corner, with the second-mode fundamental frequencies experiencing the greatest amplification. Downstream on the flare, the N-factor plot shows the most-amplified second-mode frequencies shifting gradually to higher frequencies, owing to the decreased boundary-layer thickness, until reaching  $\sim$ 400 kHz at s=460 mm. For frequencies below around 150 kHz, there is little further growth downstream of the jump at the corner.

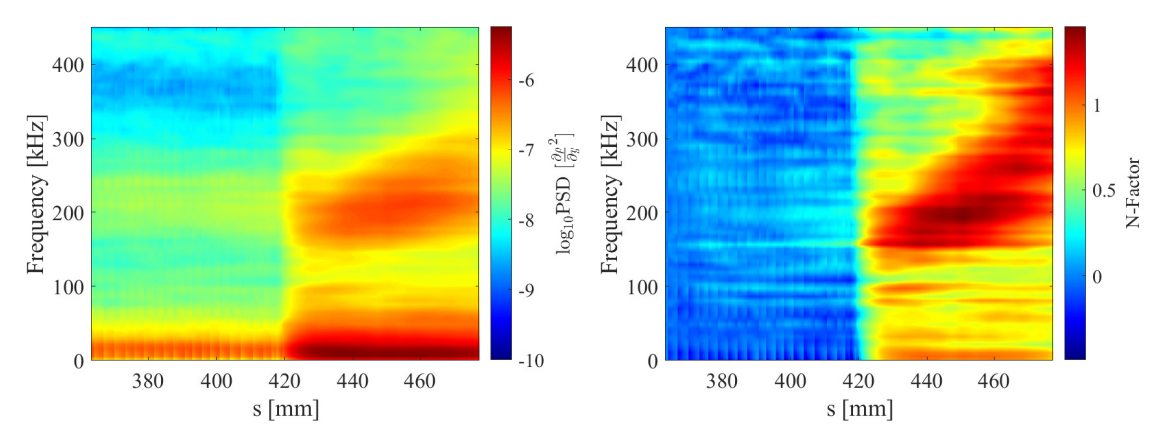


Fig 8. (Left) PSD and (right) N-factor maps along the second-mode pseudo-streamlines for the  $+5^{\circ}$  configuration.

In figure 9, we show spatially resolved N-factors along the two pseudo-streamlines for the +15° configuration. These distributions were generated using the reconstructed data, since figures 6 and 7 have shown that this technique gives reasonable results even for low-frequency disturbances. On the shear-layer pseudo-streamline (left), the N-factor map upstream of reattachment reveals that growth is primarily restricted to the lower-frequency peak, with a most-amplified frequency that decreases from ~80 kHz near s=380 mm to ~45 kHz just upstream of reattachment. We do note, however, that the growth here is not as sustained as that seen for the +15° configuration in Butler and Laurence (2021a) (see, for example, figure 14d of this earlier work). This may indicate that amplification rates for the shear-layer disturbances decrease at higher Mach numbers, which would be consistent with the findings of Jackson and Grosch (1989a). At reattachment, we observe a sharp jump in N-factor across the entire frequency range, but with no obviously favoured frequencies further downstream (in contrast to the +5° case). The N-factor map along the separation shock pseudo-streamline (right) shows significant growth of low frequencies between 40 and 160 kHz, starting further downstream than for the shearlayer pseudo-streamline. There are two distinct lobes, one lying in the range 45-90 kHz and the second 95-160 kHz; it may be significant that the second lobe is at approximately twice the frequency of the first. The lower lobe exhibits the higher peak N-factor ( $\sim$ 1.1) and is likely related to the lower-frequency peak in the shear-layer pseudo-streamline, though starts further downstream and appears to maintain a relatively constant frequency (contrasting with the drop in frequency along the shear layer).

## 3.3. Spectral Proper Orthogonal Decomposition Analysis

In this subsection, we employ spectral proper orthogonal decomposition (SPOD) to educe coherent flow structures associated with frequencies of elevated power identified in the previous section. The SPOD algorithm employed in this analysis is described in detail in Towne et al. (2018). We are primarily concerned with the leading SPOD modes (i.e., those that exhibit the highest energy at each frequency) since these typically contain the most relevant content. For simple flows, such as over a straight cone (Sousa et al., 2023), considering only the first of these modes is typically sufficient; given the additional flow complexity associated with the current geometry, however, more than one SPOD mode may be required to represent the majority of the energy at any given frequency. The SPOD modes are computed using the method of "snapshots", where each snapshot is represented by a single image from the time-resolved reconstructed signal. The SPOD spectra are estimated using Welch's method with block sizes

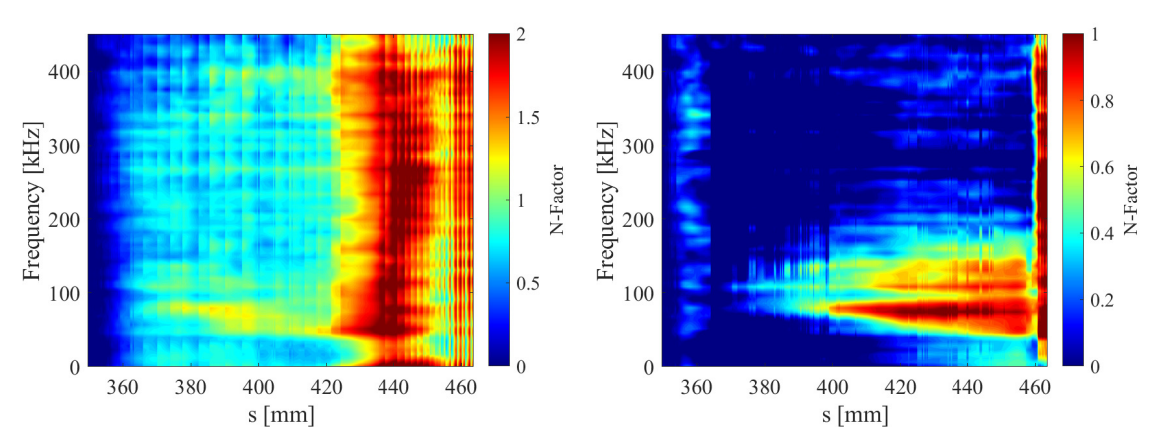


Fig 9. N-Factor maps along pseudo-streamlines of the (left) shear layer and (right) separation shock for the  $\pm 15^{\circ}$  configuration.

of length 512 and 50% overlap, and a Hamming windowing function. The total number of snapshots used for each case, along with the total number of averaged blocks and resulting frequency resolution, are presented in table 2.

Table 2. SPOD Specifications.

Flare angle	Snapshots	Blocks	Block Length	Frequency Resolution [kHz]	f <sub>max</sub> [MHz]
+5°	29,238	113	512	12.31	3.15
+15°	26,989	104	512	12.00	3.07

In figure 10, we present the leading SPOD mode shapes of three frequencies within the span of the fundamental second-mode band for the  $+5^{\circ}$  flare, encompassing the peak fundamental frequency (three leading modes) and the upper and lower sidebands (two leading modes each). For each frequency, the energy distribution of the mode 1 shapes are heavily weighted toward the structures following the compression corner, while the structures in the mode 2 shapes tend to contain more energy upstream of the corner. One potential reason for this separation of the upstream and downstream regions by the SPOD method is the distortion of the second-mode waveform through the flare shock noted earlier. In particular, upstream of the corner, the second mode maintains its characteristic rope-like structure but, downstream, the waves are substantially flatter in their top and bottom portions. This is seen more clearly in the 209 kHz mode 3 shape in figure 10: here, the energy is even more heavily concentrated upstream of the boundary layer, with the mode structure become significantly distorted after the shock, particularly in the range of s=430-450 mm. At all frequencies shown, the radiation of energy along the flare shock appears to decay slightly in mode 1 towards the end of the field of view, while modest growth is typically seen in mode 2.

In the SPOD spectrum for this condition (not shown), there were two notable regions where the modal energy percentage of the leading mode increased at higher frequencies. These two regions were centred at approximately 475 kHz and 625 kHz, indicating possible second-mode superharmonic content. The latter frequency is consistent with the second superharmonic identified earlier in the pixelwise PSDs. The former frequency is slightly higher than that observed for the first superharmonic; however, it may be that the artifact centred at 430 kHz was obscuring the true peak of the first superharmonic in the SPOD eigenspectrum. The first and second leading mode shapes at frequencies of 468 kHz and 628 kHz (the closest frequency bins to the identified peaks), are shown in figure 11. The first superharmonic exhibits similar behaviour to the fundamental disturbance, with the structured modal content for mode 1 primarily confined to within the flare boundary layer, and mode 2 exhibiting stronger content upstream of the corner. For the second superharmonic, only mode 1 shows coherent structures, with the mode

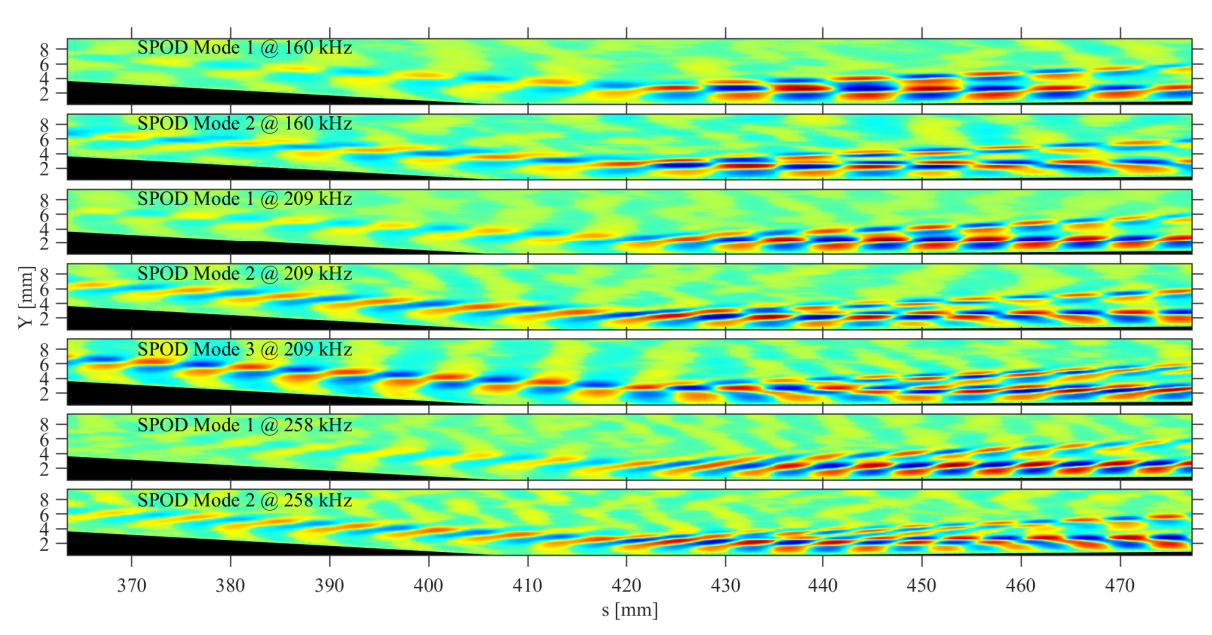


Fig 10. Leading SPOD mode shapes for frequencies 160 kHz, 209 kHz, and 258 kHz for the +5° flare.

2 content seeming mostly random and incoherent (except for  $s \gtrsim 460$  mm). The upstream content is notably less prevalent for the first harmonic than the fundamental, becoming only discernible for  $s \gtrsim 385$  mm, and is not present at all for the second superharmonic. Both superharmonics show limited radiation along the flare shock, which again rapidly decays for mode 1 but appears to grow for mode 2. We conclude that the sudden compression acts as a significant trigger for nonlinear activity within the boundary layer.

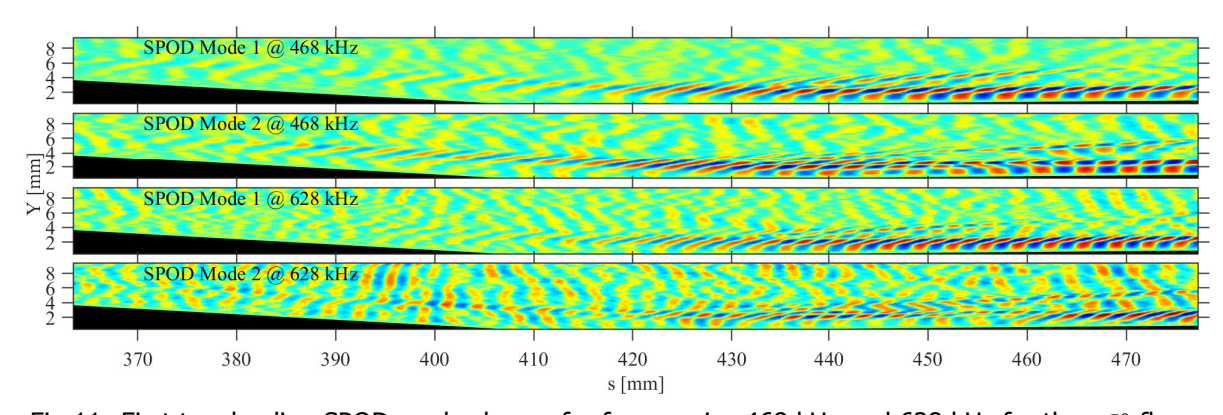


Fig 11. First two leading SPOD mode shapes for frequencies 468 kHz and 628 kHz for the  $+5^{\circ}$  flare.

Turning now to the +15° compression, figure 12 displays the first two SPOD modes for the peak fundamental second-mode frequency as well as for two sideband frequencies. The leading SPOD mode at 240 kHz shows significant amplification of waves upon passing through the separation shock. Synchronized waves can be seen bifurcating along the separation shock, where they remain at a relatively constant amplitude. The reattachment shock generates further transitory amplification of the second mode; this is followed by a rapid decay on the flare surface, particularly for SPOD mode 1 at all three frequencies. The SPOD mode 2 at each frequency exhibits the most intense radiation of energy along the reattachment shock. Note that the SPOD mode 1 of the fundamental second mode retains its characteristic rope-like structure along the majority of the shear layer, particularly for 240 kHz and 288 kHz, and also appears to undergo notable growth; this would contrast with the more neutral-type stability observed

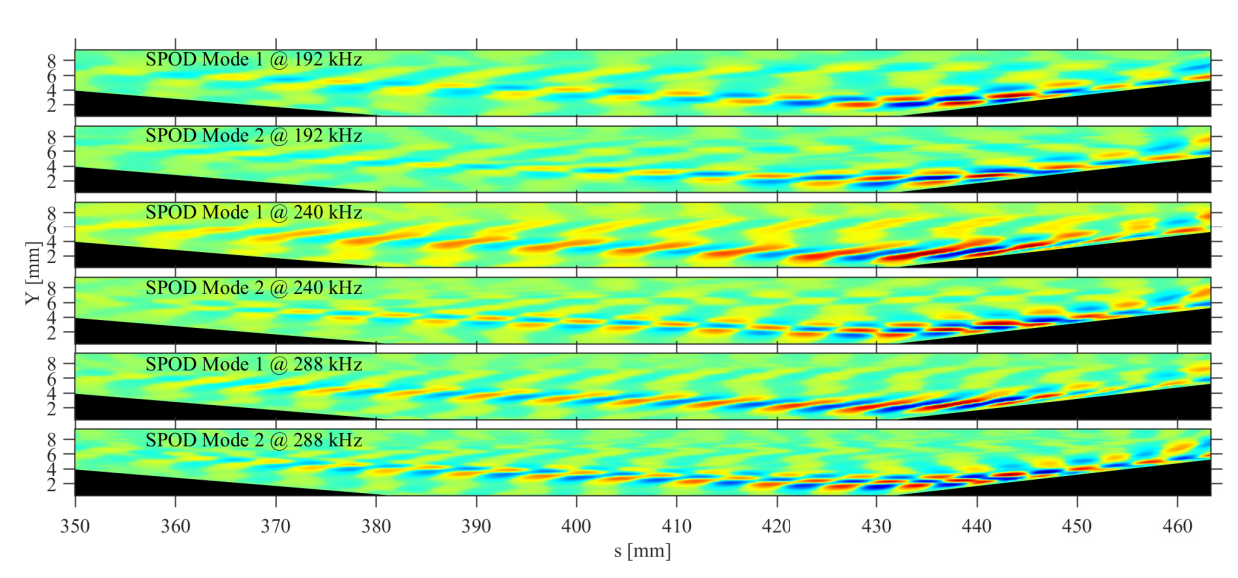


Fig 12. First two leading SPOD mode shapes for frequencies 192 kHz, 240 kHz, and 288 kHz for the  $\pm 15^{\circ}$  flare.

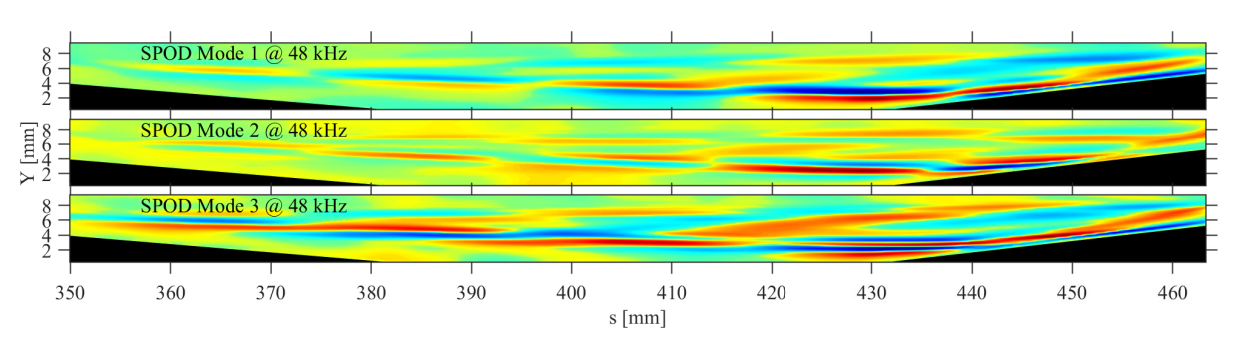


Fig 13. First three leading SPOD mode shapes at 48 kHz for the  $+15^{\circ}$  flare.

at Mach 6 (Butler and Laurence, 2022). Along the shear layer and at reattachment, the wave structures of SPOD mode 2 at these two frequencies contain waves that have additional oscillatory features in the direction normal to the cone surface. This may be related to the distortion of the second-mode waveform upon reattachment (or passage through the separation shock).

In figures 13 and 14, we show the leading three SPOD modes for the  $+15^{\circ}$  flare at frequencies of 48 kHz and 72 kHz. At the lower of these two frequencies, the first mode shape shows rapidly growing, elongated structures centred around (and aligned with) the separated shear layer. These structures can be associated with the shear-layer disturbance noted earlier and are described in detail in Butler and Laurence (2022). There is little radiation of the disturbance energy to the outer parts of the flowfield at this frequency, though we do note one outward-emanating streak originating at around s=410 mm in the third mode shape. At 72 kHz, however, much more significant radiation is observed, in both the first mode shape and even more prominently in the third. The growth of the disturbances along the shear layer, in contrast, is more subdued at this frequency (though significant amplification is seen at reattachment). This behaviour would explain the peaks observed at  $\sim$ 70 kHz on the separation shock in figures 4 and 9: the radiation from the shear layer is exciting the separation shock and producing growing perturbations at this frequency. The downstream-shifted starting point for these perturbations in figure 9 relative to the growth on the shear layer can be explained by the relatively shallow angle of the radiating structures in figure 14.

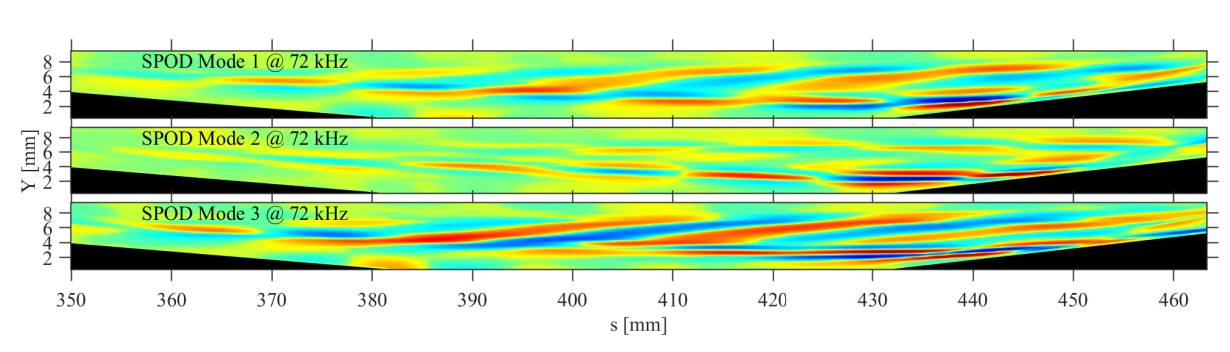


Fig 14. First three leading SPOD mode shapes at 72 kHz for the  $+15^{\circ}$  flare.

## 4. Concluding Remarks

Experiments have been conducted to investigate the development of boundary-layer and shear-layer disturbances over slender cone/flare geometries at high Mach numbers ( $\gtrsim$ 12). Two flare compression angles, +5° and +15°, allowed both attached and fully separated flowfields to be generated. A high-speed calibrated schlieren diagnostic with super-temporal reconstruction was employed, enabling global measurements over a range of frequencies encompassing all relevant disturbances.

For the +5° attached case, the unsteady flowfield was dominated by second-mode waves with frequencies near 200 kHz propagating in from the upstream boundary layer. These were amplified substantially upon interacting with the corner, with additional growth shifting to much higher frequencies; an SPOD analysis revealed the rapid onset of higher frequency superharmonics within the boundary layer on the flare. Propagation of second-mode energy along the flare shock was also noted: similar behaviour had been observed earlier for a Mach-6 flow over the same geometry, but it was significantly more prominent here. On a hypersonic vehicle, the resulting shock perturbations could have significant implications if the shock impinges on a part of the body further downstream, increasing unsteady loading and potentially reducing peak heat flux.

The separated  $+15^{\circ}$  flowfield was somewhat more complex, with both second-mode waves and lower-frequency shear-layer disturbances playing a significant role. The second-mode waves grew weakly along the separated shear layer and then underwent substantial distortion at reattachment, effectively losing their distinctive "rope-like" structure in the flare boundary layer (though still not appearing to break down to turbulence). Second-mode energy was observed propagating along both the separation and reattachment shocks. A broad range of frequencies were excited at reattachment, with no particular frequency obviously favoured for further amplification on the flare. Large amplification of shear-layer disturbances in the 30-80 kHz range occurred above the separation bubble, with the peak frequency shifting lower moving downstream. Although N-factor growth was substantial (>1), it did not appear to be as sustained as in earlier experiments at Mach 6. Another notable phenomenon associated with these shear-layer disturbances was radiation of disturbance energy to the outer portion of the flowfield at  $\sim$ 70 kHz. This radiation excited the separation shock, producing large-scale and growing perturbations of the shock structure.

In future experiments, it would be valuable to examine higher-Reynolds-number flows over the same geometries, particularly for separated flow cases. Although the flow disturbances in the present experiments had clearly entered the nonlinear regime, breakdown to turbulence was not yet observed. Given the multiple disturbance types present, it would be important to identify which is ultimately responsible for transition, potentially allowing it to be targetted with control strategies in practical flight situations.

#### References

Balakumar, P., Zhao, H., and Atkins, H. (2002). Stability of hypersonic boundary-layers over a compression corner. AIAA Paper 2002-2848.

- Balsa, T. F. and Goldstein, M. E. (1990). Inviscid spatial stability of a compressible mixing layer. Journal of Fluid Mechanics, 216:585–611.
- Benitez, E. K., Jewell, J. S., and Schneider, S. P. (2021). Propagation of controlled disturbances through an axisymmetric separation bubble at Mach 6. AIAA Paper No. 2021-2844.
- Benitez, E. K., Jewell, J. S., Schneider, S. P., and Esquieu, S. (2020). Instability measurements on an axisymmetric separation bubble at Mach 6. AIAA Paper 2020-3072.
- Butler, C. and Laurence, S. (2021a). Interaction of second-mode wave packets with an axisymmetric expansion corner. Experiments in Fluids, 62:140.
- Butler, C. S. and Laurence, S. J. (2021b). Interaction of second-mode disturbances with an incipiently separated compression-corner flow. Journal of Fluid Mechanics, 913:R4.
- Butler, C. S. and Laurence, S. J. (2022). Transitional hypersonic flow over slender cone/flare geometries. Journal of Fluid Mechanics, 949:A37.
- Casper, K. M., Beresh, S. J., Henfling, J. F., Spillers, R. W., Pruett, B. O. M., and Schneider, S. P. (2016). Hypersonic wind-tunnel measurements of boundary-layer transition on a slender cone. AIAA Journal, 54(4):1250–1263.
- Craig, S. A., Humble, R. A., Hofferth, J. W., and Saric, W. S. (2019). Nonlinear behaviour of the Mack mode in a hypersonic boundary layer. Journal of Fluid Mechanics, 872:74–99.
- Fedorov, A. (2011). Transition and stability of high-speed boundary-layers. Annual Review of Fluid Mechanics, 43:79–95.
- Fedorov, A. and Tumin, A. (2011). High-speed boundary-layer instability: Old terminology and a new framework. AIAA Journal, 49(8):1647–1657.
- Grossir, G., Dias, B., Chazot, O., and Magin, T. E. (2018). High temperature and thermal non-equilibrium effects on the determination of free-stream flow properties in hypersonic wind tunnels. Physics of Fluids, 30:126102.
- Grossir, G. and Ilich, Z. (2018). Numerical modeling of the VKI Longshot compression process. In Chazot, O. and Grossir, G., editors, Flow characterization and modeling of hypersonic wind tunnels, volume VKI Lecture Series 2018/19, chapter 2. von Karman Institute for Fluid Dynamics.
- Guiho, F., Alizard, F., and Robinet, J.-C. (2016). Instabilities in oblique shock wave/laminar boundary-layer interactions. Journal of Fluid Mechanics, 789:1–35.
- Jackson, T. and Grosch, C. (1989a). Inviscid spatial stability of a compressible mixing layer. Journal of Fluid Mechanics, 208:609–637.
- Jackson, T. and Grosch, C. (1990). Absolute/convective instabilities and the convective Mach number in a compressible mixing layer. Physics of Fluids A: Fluid Dynamics, 2(6):949–954.
- Jackson, T. L. and Grosch, C. E. (1989b). Inviscid spatial stability of a compressible mixing layer. Journal of Fluid Mechanics, 208:609–637.
- Kennedy, R. E., Laurence, S. J., Smith, M. S., and Marineau, E. C. (2018). Investigation of the second-mode instability at Mach 14 using calibrated schlieren. Journal of Fluid Mechanics, 845:R2.
- Laurence, S., Wagner, A., and Hannemann, K. (2016). Experimental study of second-mode instability growth and breakdown in a hypersonic boundary layer using high-speed schlieren visualization. Journal of Fluid Mechanics, 797:471–503.
- Lees, L. and Lin, C. C. (1946). Investigation of the stability of the laminar boundary layer in a compressible fluid. NACA TN 1115.
- Lugrin, M., Beneddine, S., Leclercq, C., Garnier, E., and Bur, R. (2020). Transition scenario in hypersonic axisymmetrical compression ramp flow. Journal of Fluid Mechanics, 907:1–40.

- Mack, L. M. (1975). Linear stability theory and the problem of supersonic boundary-layer transition. AIAA Journal, 13(3):278–289.
- Novikov, A., Egorov, I., and Fedorov, A. (2016). Direct numerical simulation of wave packets in hypersonic compression corner flow. AIAA Journal, 54(7):2034–2050.
- Paredes, P., Scholten, A., Choudhari, M. M., Li, F., Benitez, E. K., and Jewell, J. S. (2022). Boundary-layer instabilities over a cone–cylinder–flare model at Mach 6. AIAA Journal, 60(10):5652–5661.
- Parziale, N. J., Shepherd, J. E., and Hornung, H. G. (2014). Free-stream density perturbations in a reflected-shock tunnel. Experiments in Fluids, 55(2):1665.
- Roghelia, A., Olivier, H., Egorov, I., and Chuvakhov, P. (2017). Experimental investigation of Gortler vortices in hypersonic ramp flows. Experiments in Fluids, 58(139).
- Saric, W. S. (1994). Görtler vortices. Annual Review of Fluid Mechanics, 26(1):379–409.
- Sidharth, G., Dwivedi, A., Candler, G., and Nichols, J. (2018). Onset of three-dimensionality in supersonic flow over a slender double wedge. Physical Review Fluids, 3(093901).
- Sousa, C., Kennedy, R., King, R., Bathel, B., Weisberger, J., and Laurence, S. (2023). Global analysis of nonlinear second-mode development in a Mach-6 boundary layer from high-speed schlieren data. Experiments in Fluids, 65:19.
- Sousa, C. and Laurence, S. (2025). Super-temporal global reconstruction of convective disturbances from images of two-dimensional flows. Experiments in Fluids, 66:90.
- Towne, A., Schmidt, O., and Colonius, T. (2018). Spectral proper orthogonal decomposition and its relationship to dynamic mode decomposition and resolvent analysis. Journal of Fluid Mechanics, 847:821–867.
- Unnikrishnan, S. and Gaitonde, D. V. (2020). Linear, nonlinear and transitional regimes of second-mode instability. Journal of Fluid Mechanics, 905:A25.
- Zhuang, M., Kubota, T., and Dimotakis, P. E. (1988). On the instability of inviscid, compressible free shear layers. AIAA Paper No. 88-3538.